PHYSICAL REVIEW B **85**, 085416 (2012)

Metal-dielectric-metal surface plasmon-polariton resonators

Anu Chandran, Edward S. Barnard, Justin S. White, and Mark L. Brongersma
Geballe Laboratory for Advanced Materials, Stanford University, Stanford, California 94305, USA

(Received 2 August 2011; revised manuscript received 10 November 2011; published 9 February 2012)

A theoretical study of standing-wave resonances of surface plasmon polaritons (SPPs) in finite-length metal-dielectric-metal cavities is presented. A Fabry-Pérot model is constructed to describe the cavity resonances, and the associated optical parameters are calculated analytically. One key parameter is the phase acquired by resonating SPPs upon reflection from cavity end faces. This phase pickup is associated with the near-field energy storage at these end faces, and the imaginary part of the reflection coefficient is shown to be approximately proportional to the stored energy. Using the Fabry-Pérot model, we also calculate the transmission cross section, peak position, as well as the Q factor of the cavity, and we find good agreement with full-field numerical simulations for a wide range of wavelengths and device dimensions.

DOI: 10.1103/PhysRevB.85.085416 PACS number(s): 73.20.Mf, 42.82.Et, 42.25.Bs

I. INTRODUCTION

Plasmonic cavities allow deep subwavelength modes with high field concentration, and are therefore very attractive for small footprint active nanophotonic devices. The possibility of concentrating light into a nanoscale volume has a profound effect on the efficiency of linear and nonlinear optical processes, which often scale with the ratio of the optical quality factor Q to the mode volume V_m. Despite their modest quality factors (typically between 10 and 100), metallic cavities can have such small mode volumes that they can outperform much higher Q dielectric microcavities ($Q \sim 10^6$). As such, they have been proven useful for a variety of applications, including single molecule sensing,[1] spectroscopy,[2,3] optical trapping,[4] surface enhanced reactions,[5,6] spontaneous emission modification,[7–10] surface plasmon-polariton (SPP) modulators,[11–14] and SPP sources.[15,16]

Finite-length metal-dielectric-metal (MDM) cavities have attracted particular attention for their ability to concentrate light to nanoscale dimensions[17] through the excitation of wavelength-tunable cavity resonances.[18] The high field intensity in the dielectric region makes these structures well-suited for active plasmonic structures. MDM plasmonic slits have also been shown to enhance optical absorption within materials adjacent to the MDM end face.[19,20] The relative ease of fabricating the MDM structures together with the possibility of using the metal layers as electrical contacts also make this geometry well-suited for optoelectronic applications.[11,16,21,22]

Plasmonic cavities are most readily studied with full-field simulations, which, although exact, do not lend themselves to a clear physical interpretation. The resonant optical properties of wavelength-scale plasmonic antennas and cavities are most easily understood if seen as truncated waveguides supporting SPPs with a well-defined λ_{SPP}.[23–25] In such finite-sized structures, the SPPs undergo reflections from the end faces, and the constructive interference of multiply reflected SPPs can give rise to Fabry-Pérot resonances.[24,26] The optical quality factor associated with the resonances is determined by the SPP reflection amplitude as well as propagation losses. On the other hand, λ_{SPP} and the phase acquired upon reflection from the end faces determine the resonant length, L_{res}, of the cavity. This point follows directly from the resonance condition that the round-trip phase for SPPs must be an integer multiple of 2π. It has been shown that plasmonic resonators can exhibit large reflection phases, and in these cases our microwave intuition that suggests a resonance length of $\frac{m\lambda}{2}$ is insufficient.[23,24,27,28]

From the above discussion, it is clear that a quantitative prediction of MDM cavity resonances requires knowledge of the reflection phase and amplitude. The problem of SPP reflection has been extensively studied in the past for single interface surface plasmons with various dielectric[29] and metallic[30] discontinuities and thin dielectric overlayers.[31] An exact analytical treatment of SPP reflection in multilayer structures is complicated by the presence of multiple SPP modes in addition to the bulk propagating and evanescent modes. Calculation of SPP waveguide modes along finite-width metallic stripe waveguides by using an effective index model has been done before,[32] but this framework is not ideally suited to the problem at hand, in which SPPs run into an abrupt termination of a waveguide. It has been shown that for a metallic rod antenna, an approximation for this phase pickup with a factor for the finite reactance of the rod end faces correctly predicts the resonance wavelengths.[24] Recently, numerical calculations of the reflection amplitude and phase for a terminated metal sheet have been made using full-field simulations, and these were used successfully to predict the resonant properties of stripe antennas (truncated DMD waveguides).[28] These calculations are in reasonable agreement with recent experiments.[27] For MDM cavities, analytical calculations of the reflection phase exist for lossless and dispersion-free metals,[33] but an extension to real metals would be of value.

In this paper, we start by calculating analytically the reflection coefficient and phase acquired by SPPs upon reflection from the cavity end face using a simple mode-matching model for real metals exhibiting both dispersion and loss. Our approach is similar to that in Refs. 33 and 34, but it employs an intuitive energy conservation boundary condition in addition to the field matching at the cavity termination. The model clearly demonstrates the origin of the reflection phase as arising from coupling to the evanescent, near-field modes in the free-space region. We also show that the imaginary part of the reflection coefficient is approximately proportional to the energy stored in the near field of the MDM cavity end face. The calculations demonstrate that by choosing the right dielectric thickness, it is possible to maximize this near-field energy stored, resulting in a high electric field intensity in that region. With knowledge of the excitation and reflection coefficients, we finally also calculate analytically the transmission cross section and the quality factor (Q) of finite-length MDM cavities with real material properties including losses. Comparison with full-field finite-difference simulations shows that the model can very accurately predict the resonance behavior of MDM cavity structures for a wide range of dielectric thicknesses and cavity lengths. The design of a plasmonic device for operation at a particular wavelength, accounting for the SPP dispersion and scattering, will require the use of full-field simulations. However, an analytical model that captures the essential details of surface plasmon resonance conditions in these devices can serve as a good design rule and further our understanding of the physics of SPP reflections in MDM devices. This would enable the leveraging of familiar concepts and designs from other areas, such as microwave and radiofrequency circuits.

II. SPP MODES OF MDM STRUCTURES

Figure 1 shows a schematic of the truncated MDM waveguide resonator that is investigated in this paper. It consists of two infinitely thick metallic layers separated by a thin dielectric region, through which power is guided in an MDM or gap SPP mode. The thickness of the dielectric is denoted by d_{ins} and the SPPs propagate in the x direction. The dielectric and the metal dielectric constants are denoted by ϵ_d and ϵ_m, respectively.

It is important to understand the dependence of the wavelength and propagation loss of the allowed SPPs in the MDM cavity as they determine the resonant cavity lengths and the associated quality factors. SPP modes in planar MDM structures have been extensively studied in the past.[35–39] In general, these waveguides support SPP modes with both symmetric and antisymmetric field profiles (H_y field), but for sufficiently thin dielectrics, only the mode with a symmetric field profile is allowed; such structures are considered here. Also, the symmetry of the structure prevents mixing between the modes at the reflective cavity termination. For this reason, only the symmetric mode is included in this study. The validity of using only this mode will be verified by full-field simulations. As the dielectric thickness d_{ins} is reduced, the mode index as well as the propagation loss for the symmetric mode increase. It is clear that the increased lateral mode confinement comes at the cost of lowered SPP propagation length. This in turn could affect the Q in the regime where the losses are dominated by propagation losses rather than reflection losses. A detailed analysis of the variation in SPP dispersion with the structure dimensions can be found in Ref. 38.

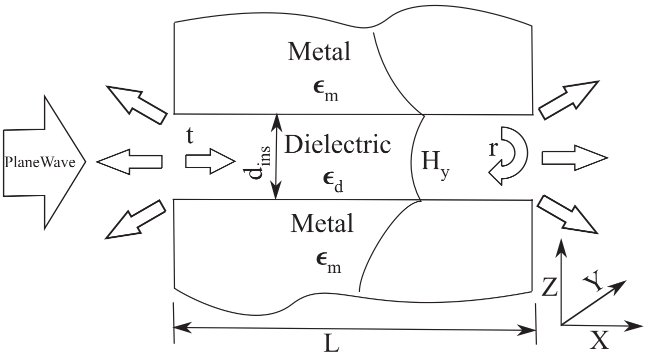

FIG. 1. Schematic of a finite-length MDM cavity. The H_y-field profile of the symmetric SPP mode is shown.

In the following section, we look at resonances in finite-length MDM cavities, ascribing them to constructive interference of field symmetric modes reflected from the cavity end faces. We assume that the field inside the MDM cavity can be described only using forward propagating and reflected SPPs. In addition to the propagating modes, the structure also supports a continuum of evanescent (in the propagation direction) modes, which are required for a complete description of the fields inside the cavity.[40] Such local modes are important near terminations of waveguides and compact cavities. We assume that the contribution of these modes on the SPP reflection coefficient can be ignored. No assumption is made regarding the nature of the fields outside the cavity. We look at resonance properties in the visible to near-infrared frequency range for very thin dielectric MDM cavities. The theory is developed assuming infinite metal outer layer thickness and a small dielectric thickness. Only an outline of the derivation is included here. A more detailed description of the steps involved can be found in Appendix A.

A. Transmission into the cavity

In this section, we explore the coupling of a normally incident, transverse magnetic (TM) plane wave, $H = (0, H_y, 0)$, with a free-space wavelength λ, into an MDM cavity Fig. 1. The wave that is transmitted into the cavity is assumed to be a symmetric gap SPP. The reflected light is described by a continuum of waves moving back away from the cavity. From the continuity of the E_z field, we then find

$$E_z^{\mathrm{pw}} + E_z^{\mathrm{ref}} = t E_z^{\mathrm{sp}}. \tag{1}$$

Here, t is the amplitude of the forward propagating symmetric SPP electric field E_z^{sp} and can be viewed as an SPP excitation coefficient. By assuming unity amplitude for the incoming plane-wave field, E_z^{pw}, and expanding the reflected field, E_z^{ref}, into a continuum of plane-wave modes with amplitude $g(k)$, Eq. (1) can be rewritten as

$$1 + \int_{-\infty}^{\infty} g(k) e^{ikz} dk = t E_z^{\mathrm{sp}}. \tag{2}$$

By taking the Fourier transform of Eq. (2), we get

$$g(u) = \frac{t}{2\pi} \int_{-\infty}^{\infty} E_z^{\mathrm{sp}} e^{-ik_0 uz} dz - \delta(u), \tag{3}$$

where k is written as $k_0 u$ with $k_0 = \frac{2\pi}{\lambda}$ and δ is the Dirac impulse.

In addition to the field continuity equation, we need another boundary condition to calculate t, the SPP excitation coefficient. One physically meaningful boundary condition is the continuity of the total integrated x-directed Poynting flux passing through the y-z plane at the cavity termination. As the system is translationally invariant along the y direction, this boundary condition can be expressed in terms of integrals along the z direction. With this, we get

$$\int_{-\infty}^{\infty} dz\big(E_z^{\mathrm{pw}} + E_z^{\mathrm{ref}}\big)\big(H_y^{\mathrm{pw}} + H_y^{\mathrm{ref}}\big)^* = tt^* \int_{-\infty}^{\infty} dz\, E_z^{\mathrm{sp}} H_y^{\mathrm{sp}^*}. \tag{4}$$

Here, $*$ denotes the complex conjugate of the quantity. Simplifying Eq. (4) with Eq. (2) and solving for t, we arrive at the following expression:

$$t = \left(\frac{2I_1(0)\sqrt{\frac{\epsilon_0}{\mu_0}}}{\frac{1}{\lambda}\sqrt{\frac{\epsilon_0}{\mu_0}} \int_{-\infty}^{\infty} du \frac{|I_1(u))^2|}{\sqrt{1-u^2}} - \int_{-\infty}^{\infty} dz\, E_z^{\mathrm{sp}} H_y^{\mathrm{sp}*}} \right)^*, \tag{5}$$

where

$$I_1(u) = \int_{-\infty}^{\infty} E_z^{\mathrm{sp}} e^{-ik_0 uz} dz. \tag{6}$$

B. Calculation of the SPP reflection coefficient

Figure 1 also schematically indicates the SPP reflection process, which is considered next. It shows how a symmetric SPP mode is incident from the left and propagates toward the cavity termination on the right. Upon reflection from the end face, a backward propagating SPP is generated together with a continuum of forward propagating plane waves, E^{fs}, outside of the cavity. Again, we can write a continuity equation for the electric field, which looks as follows:

$$(1+r)E_z^{\mathrm{sp}} = E_z^{\mathrm{fs}}. \tag{7}$$

By balancing the total Poynting flux through the y-z plane at the cavity termination, we obtain

$$(1+r)(1-r^*) \int_{-\infty}^{\infty} dz\, E_z^{\mathrm{sp}} \big(H_y^{\mathrm{sp}}\big)^* = \int_{-\infty}^{\infty} dz\, E_z^{fs} \big(H_y^{\mathrm{fs}}\big)^*. \tag{8}$$

Using the same simplifications as in the calculation of the excitation coefficient, and expanding the free-space transmitted electric field into a continuum of plane waves, we arrive at the following expression for the reflection coefficient:

$$\frac{1-r^*}{1+r^*} = \frac{1}{\lambda\sqrt{\frac{\mu_0}{\epsilon_0}} \int_{-\infty}^{\infty} dz\, E_z^{\mathrm{sp}} H_y^{\mathrm{sp}*}} \times \int_{-\infty}^{\infty} du \frac{-|I_1(u)^2|}{\sqrt{1-u^2}}. \tag{9}$$

A detailed derivation of the reflection coefficient is included in Appendix A.

C. Cavity properties

In this section, we discuss cavity properties of interest and how they can be determined from the SPP behavior described in the previous sections. One of the key properties of a cavity that can be verified experimentally is the total transmitted power through the cavity, P_{out}. This quantity can be derived analogous to that of a conventional Fabry-Pérot cavity as[41]

$$P_{\mathrm{out}} = \left| \frac{t e^{i\beta L}}{1 - r^2 e^{2i\beta L}} \right|^2 \int_{-\infty}^{\infty} dz\, E_z^{\mathrm{sp}} H_y^{\mathrm{sp}*} (1 - |r|^2). \tag{10}$$

The spectral behavior of P_{out} near a resonance can be approximated by a Lorentzian line shape centered at an angular frequency ω_0 and whose full width at half maximum, $\Delta\omega$, is determined by the optical quality factor for the cavity,

$$Q = \frac{\omega_0}{\Delta\omega}. \tag{11}$$

We can also define a transmission efficiency for a finite-length cavity by normalizing P_{out} to the power coupled into a cavity as

$$T_{\mathrm{eff}} = \left| \frac{e^{i\beta L}}{1 - r^2 e^{2i\beta L}} \right|^2 (1 - |r|^2). \tag{12}$$

From Eq. (12), it can be seen that the cavity transmission efficiency has a maximum when $re^{i\beta L}$ is purely real. This resonance condition provides an expression for the resonance length of the cavity:

$$L_{\mathrm{res},m} = \frac{m\pi - \phi}{\pi} \frac{\lambda_{\mathrm{SP}}}{2}, \tag{13}$$

where $m = 1,2,3, \ldots$ is the order of the resonance and ϕ is the phase of the reflection coefficient such that $r = |r|e^{i\phi}$.

D. Origin of the reflection phase

The phase pickup on reflection is critically important when determining the resonant wavelengths of the MDM cavity. The origin of this phase pickup, which is present even in a perfect electrical conductor (PEC),[42] is related to the small metal-to-metal spacing. When the size of the aperture is small compared to the wavelength of light, there is a substantial transmission to evanescent diffraction orders. This can be seen clearly if we simplify Eq. (8). By substituting the expressions for the free-space fields and normalizing the field profiles such that the incident time-averaged SPP Poynting flux is unity, we find

$$(1+r)(1-r^*) = \frac{|(1+r)|^2}{2\lambda\sqrt{\frac{\mu_0}{\epsilon_0}}} \int_{-\infty}^{\infty} du \frac{|I_1(u)|^2}{\sqrt{1-u^2}}. \tag{14}$$

Splitting the reflection coefficient r into its real and imaginary parts gives

$$r = r_{\mathrm{re}} + i r_{\mathrm{im}}. \tag{15}$$

Substituting for r on the left-hand side of Eq. (14) and simplifying, we obtain

$$1 - |r|^2 + 2i r_{\mathrm{im}} = \frac{|(1+r)|^2}{2\lambda\sqrt{\frac{\mu_0}{\epsilon_0}}} \int_{-\infty}^{\infty} du \frac{|I_1(u)|^2}{\sqrt{1-u^2}}. \tag{16}$$

As expected, the real part of the integrated time-averaged power flow through the interface, $(1 - |r|^2)$, corresponds to the propagating ($|u| \leqslant 1$) field components. Also, the contribution to the imaginary part of the reflection coefficient comes entirely from the arm of the integral with $|u| > 1$, the evanescent components. From the definition of time-averaged Poynting flux,[43] this is proportional to the difference between the stored magnetic and electric energies in the near field. We have for harmonic time varying fields,

$$W_e = \frac{1}{4}\int_V E \cdot D^* dV \qquad (17)$$

$$W_m = \frac{1}{4}\int_V B \cdot H^* dV \qquad (18)$$

$$\oint_C S \cdot n dA + 2i\omega(W_e - W_m) = 0, \qquad (19)$$

where W_e and W_m are the energies stored in the electric and magnetic fields, respectively. S is the time-averaged Poynting flux. Here V is the volume under consideration and C is the area of the closed surface enclosing it with an outward normal n. If the volume V is chosen as the semi-infinite half-space ahead of the MDM structure, the imaginary part of the Poynting flux has contributions only from the input face (y-z plane) near the cavity termination. With this, we get

$$-2ir_{\text{im}} + 2i\omega(W_e - W_m) = 0, \qquad (20)$$

$$\frac{r_{\text{im}}\lambda}{2\pi c} = W_e - W_m = \frac{|1+r|^2\epsilon_0}{4\pi} \times \int_{u=1}^{\infty} \frac{|I_1(u)|^2}{\sqrt{u^2-1}} du. \qquad (21)$$

Even though the imaginary part of the reflection coefficient is directly related to the difference in the electric and magnetic energy, the quantity of interest in most situations is the total near-field energy stored. High energy storage in the electric near field could lead to a higher electric field intensity in the near-field region of the cavity. Energy stored in the electromagnetic field is not usually an easy quantity to calculate, but in this case we can easily decompose the total electromagnetic field in front of the cavity into normal modes and sum up the energy in each mode. The total energy, including that of the propagating modes, is obviously infinite, but if we only consider the near-field contribution we get, after a straightforward calculation (for more details, see Appendix B),

$$W_e + W_m = \frac{|1+r|^2\epsilon_0}{4\pi} \int_{u>1}^{\infty} \frac{|I_1(u)|^2}{\sqrt{u^2-1}} \times \left(1 + \frac{1}{u^2-1}\right) du. \qquad (22)$$

The integral blows up at $u = 1$ due to the second term in the large parentheses. This term decays very fast for larger u, contributing to the integral only very near $u = 1$, and hence these correspond to waves with very slow spatial decay away from the cavity. This energy contribution, though substantial, is of limited interest as the fields are not localized near the cavity. If we are only interested in the rapidly decaying high-intensity near fields in front of the cavity, we can neglect that term and write an approximate expression for the energy stored in the near field of the cavity as

$$W_{\text{NF}} \approx \frac{|1+r|^2\epsilon_0}{4\pi} \int_{u=1}^{\infty} \frac{|I_1(u)|^2}{\sqrt{u^2-1}} du. \qquad (23)$$

This is equal to the difference in the stored electric and magnetic energy. From Eq. (21), we can thus obtain a very simple expression of the energy stored in the near field in terms of the imaginary part of the reflection coefficient:

$$W_{\text{NF}} = \frac{r_{\text{im}}\lambda}{2\pi c}. \qquad (24)$$

We find that the imaginary part of the reflection coefficient is directly proportional to the near-field energy stored at the cavity termination.

E. Model validation

The above-described intuitive model for MDM cavity resonances involves several simplifications in terms of the exact field distributions throughout the structure. In order to have complete field matching at all points along the cavity edges, we need, in addition to the propagating modes in the cavity, a continuum of evanescent modes that exist in the cavity as well as laterally propagating (along the z direction) SPP modes at the cavity edge surface.[40] The simplification ignoring the evanescent modes inside the cavity will lead to some error in the field calculations, but since these modes are not expected to transmit energy in the direction of propagation for sufficiently long cavities, we expect that the energy-matching method will lead to a reasonably accurate calculation of the relevant quantities. Also, the generation of laterally propagating SPPs is expected to be most efficient at higher dielectric thicknesses than what is mostly considered in this study.[44] It is expected that the approximations made are more valid in cases in which the metal properties and the structure dimensions favor the simplifications involved. For example, ignoring the finite penetration of the plane wave at the in-coupling face in the transmission coefficient calculation will be a good approximation at longer wavelengths where the metal has a large negative dielectric constant. In order to check the validity of the assumptions, for our cavity geometries and our choice of metal (Ag), we compared the results with those obtained from full-field finite-difference frequency domain (FDFD) simulations.[45] In all cases analyzed in Sec. III, we see excellent agreement between the two, confirming the validity of the assumptions.

III. NUMERICAL RESULTS

In this section, we explore the dependence of the cavity properties on the different cavity parameters, such as d_{ins}, ϵ_m, L, λ, etc. This dependence is somewhat complicated by the frequency dependence of the materials response. In order to understand the effects of each of these variables separately, we first look at the variation in the magnitude and phase of the reflection coefficient with the normalized insulator thickness $\frac{d_{\text{ins}}}{\lambda}$ for various wavelength-independent values of the metal dielectric constant.

As shown in Fig. 2(a), the reflection coefficient magnitude ($|r|$) increases as the cavity dielectric thickness is reduced, and the metal dielectric constant moves toward resonance ($\epsilon_m \to -1$). This can be attributed to two main factors: a higher effective-index contrast due to the increasing gap SPP mode index, and an increased mode mismatch due to tighter vertical confinement of the mode. On the other hand, the phase pickup on reflection, shown in Fig. 2(b), increases as the metal properties move toward resonance and decreases on reducing the cavity dielectric thickness.

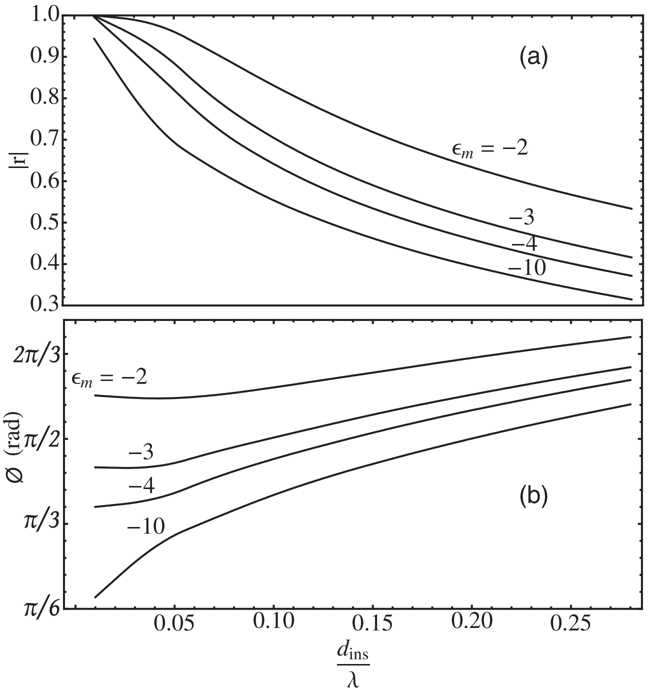

FIG. 2. $|r|$ and ϕ (phase) for different values of ϵ_m as a function of scaled dielectric thickness.

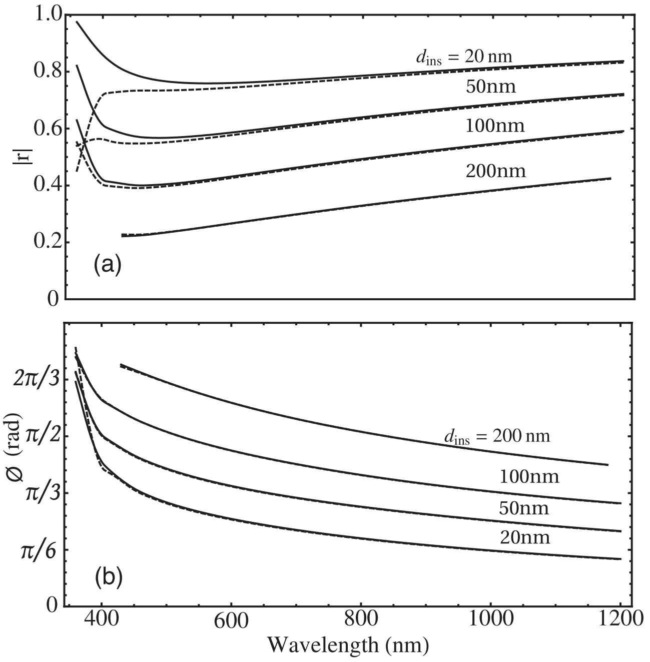

FIG. 3. Reflection amplitude $|r|$ and ϕ (phase) for an Ag-air-Ag MDM structure as a function of wavelength for different d_{ins} values. Solid lines: without loss. Dotted lines: with loss.

The electric energy stored is greater than the magnetic energy as seen from the positive sign of r_{im} $(0 \leqslant \phi \leqslant \pi)$. Thus the cavity end faces have associated with them a finite capacitance, which originates from excitation of the evanescent modes in the free-space region.

When the cavity thickness d_{ins} decreases, the near-field energy stored is lower and the reflection phase decreases. For real metals supporting SPPs, there is, in addition to the aperture effect, a contribution from the evanescent nature of the SPP mode profile into the metal. When $|\epsilon_m|$ decreases, the SPP extends further into the metal, resulting in a higher coupling to the free-space evanescent modes, and we get high near-field energy ahead of the cavity, which increases the reflection phase.

Next, we explore the reflection properties for a cavity metal with wavelength-dependent material properties. The calculations are done for silver (Ag), and its material properties for the metal are taken from Rakic *et al.*[46] In our study, we consider Ag with and without loss. Lossless material properties are obtained by considering only the real part of the dielectric constant. Figure 3 shows the variation of the reflection coefficient magnitude and phase as a function of wavelength for different cavity dielectric thicknesses. The lossless case is plotted with solid lines and the case with loss is shown with dashed lines. Clearly evident is the presence of two regimes in the variation of the reflection coefficient magnitude as a function of wavelength. As seen in Fig. 3(a), the cavity truncation becomes a better reflector near the surface plasmon resonance frequency (short wavelength). On increasing wavelength, $|r|$ goes through a minimum, which is the result of two competing factors that contribute to the reflection. At short wavelengths, the rapid variation in the mode index with wavelength due to a change in ϵ_m determines the behavior of r. So $|r|$ decreases with increasing wavelength. But for larger wavelengths, the cavity termination, which acts as a radiating antenna, becomes less effective due to the size mismatch between the free-space wavelength and the SPP mode, increasing the reflection coefficient. Together, these two competing factors result in a minimum in the magnitude of the reflection coefficient. The introduction of losses [dotted line in Fig. 3(a)] changes the short-wavelength characteristics of the cavity. In a lossy MDM structure, the mode index does not rise as high as in the lossless case at short wavelengths. Consequently, the low index and the decreased vertical confinement lead to a decrease in the reflection coefficient magnitude. At longer wavelengths, losses are negligible as the SPP mode is pushed out of the metal, and the reflection characteristics are similar to the lossless case. On the other hand, the reflection phase [Fig. 3(b)] decreases monotonically with increasing wavelength and is larger for a thicker insulating spacer in the cavity. The phase pickup is almost unaffected by the introduction of losses in the metal, even very close to the surface plasmon resonance frequency. This fact is interesting from a device design perspective as it facilitates easy design rules for resonant cavity devices without introducing the complexity of loss at a given wavelength.

The near-field energy stored in front of the cavity, W_{NF}, is proportional to λr_{im}. Figure 4 shows a plot of λr_{im} as a function of d_{ins} for different free-space wavelengths. We see that for longer wavelengths, there exists a maximum in the near-field energy. The near-field energy storage in front of the cavity is the result of mode mismatch and coupling to the evanescent modes. For a low reflection coefficient with little mode mismatch there is very little energy stored in the near field. Hence for large dielectric thickness with low $|r|$, near-field energy storage decreases with increasing dielectric thickness. The increase in near-field energy storage

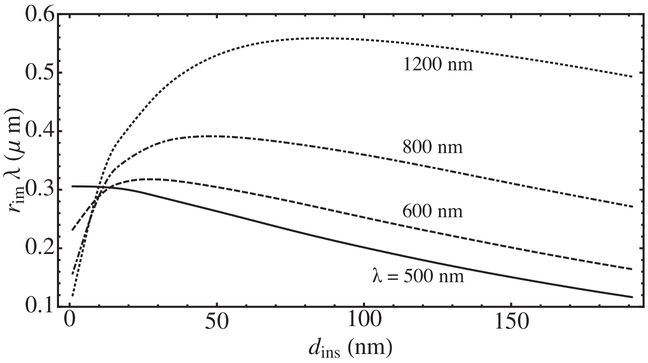

FIG. 4. $r_{\text{im}}\lambda$ for Ag-air-Ag cavity for different d_{ins}.

with wavelength in the large insulator thickness regime is also the result of increasing $|r|$. But for small dielectric thickness, the contribution from the evanescent mode profile is larger for smaller λ, resulting in higher energy storage. The existence of the maximum for a given wavelength allows us to tune the cavity to have larger near fields at a wavelength of choice. This can be of importance for applications where high local fields are desired, such as surface plasmon Raman spectroscopy. This maximum arises from a single reflection event at the cavity termination and is different from the cavity resonance of the finite-length cavity.

The transmission efficiency of the cavity, as defined in Eq. (12), will be considered next. This quantity can be obtained from experiments and is most directly linked to the fundamental optical processes associated with the cavity. Shown in Fig. 5 is the transmission efficiency of a lossy Ag cavity as a function of wavelength for a dielectric thickness $d_{\text{ins}} = 20$ nm and for different cavity lengths. The plot shows the cavity resonances, which move to longer wavelengths as the cavity length is increased. The results from full-field FDFD calculations are also plotted in the figure, showing excellent agreement with the analytical calculations.

The cavity resonance length (L_{res}) for different resonance orders, as a function of dielectric thickness, is plotted in Fig. 6. The good correspondence between the analytical calculation and the full-field simulations confirms the validity of our model for the considered parameters. From the figure it can be seen that the resonant length calculations made by ignoring the phase pickup on reflection (dotted lines) would result in substantial error, especially at higher dielectric thicknesses.

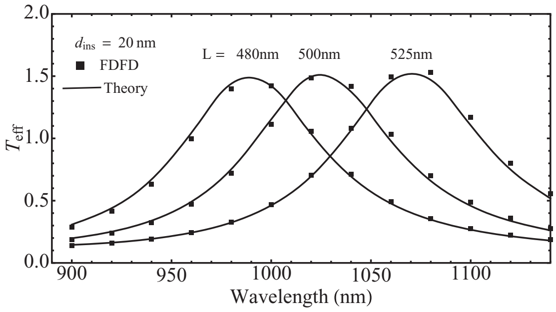

FIG. 5. Transmission efficiency (T_{eff}) through an Ag-air-Ag cavity for different cavity lengths (L) as a function of wavelength.

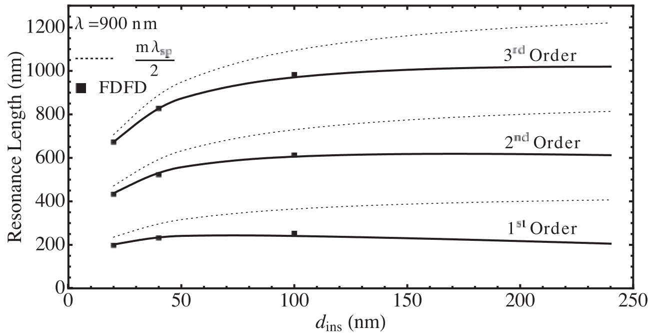

FIG. 6. Cavity resonance length as a function of dielectric thickness for different orders. Free-space wavelength $\lambda = 900$ nm. (Ag-air-Ag cavity with loss.)

Another interesting feature in the plots is the relatively weak dependence of the resonance length on the dielectric layer thickness for sufficiently large thicknesses ($>$ 50 nm). This can be understood from Eq. (13), which shows that the resonance length is dependent on two factors: (i) the gap SPP wavelength and (ii) the phase pickup on reflection. As the dielectric layer thickness is increased, the gap SPP wavelength increases and approaches that of the single interface mode. As the same time, the reflection phase also increases. As the effects of an increased wavelength and phase work in opposite directions, the resonant length stays more or less the same.

As the dielectric thickness is reduced in an MDM cavity, the symmetric SPP mode is more confined, resulting in a very small mode volume. This is very advantageous for active plasmonic devices, allowing, for example, efficient coupling of quantum emitters to SPP gap modes in MDM cavities.[7] Strong emission rate enhancement is also predicted even for nonresonant conditions in an infinite-length MDM slab geometry.[47] The transmission cross section can be used to calculate the quality factor (Q) of the finite-length MDM cavities. Shown in Fig. 7 is a plot of Q versus cavity length for different dielectric thicknesses at $\lambda = 800$ nm for an Ag-air-Ag MDM cavity with metal losses included. The cavity Q increases with length, showing evidence of being reflection loss limited. This is true even for dielectric thickness as low as 10 nm with cavity lengths as large as 1500 nm, demonstrating that propagation loss is not the dominating loss mechanism in these cavities. This suggests the possibility of increasing the

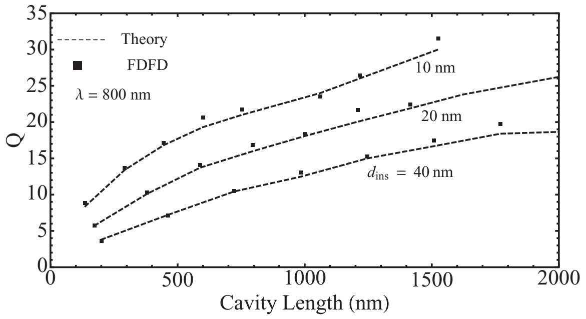

FIG. 7. Q factor of the cavity vs cavity length for different dielectric thicknesses. Free-space wavelength $\lambda = 800$ nm. (Ag-Air-Ag cavity with loss.)

quality factor of these cavities further by end face shaping, thus realizing very low reflection losses. Such a device will exhibit larger Q/V values and enable very effective coupling of optical emitters to a well-defined SPP mode.

IV. CONCLUSION

In conclusion, we have developed a fully analytical theory for SPP resonances in finite-length MDM cavities. It builds on previous results that indicate that a variety of wavelength-scale plasmonic systems can be viewed as resonators for SPPs.[23,24,28] Such a model requires knowledge of the basic optical properties of SPP modes supported by an extended MDM waveguide and the SPP reflection and transmission properties at the termination of such a waveguide. We have presented an analytical framework to determine these properties for cavities consisting of real metals exhibiting loss and dispersion. Similar to what was found for other wavelength-scale plasmonic cavities, these calculations predict a substantial phase pick up by the SPP upon reflection from the cavity end faces. We showed that the origin of this phase pick up lies in the excitation of evanescent modes in the free-space region just outside the cavity. Furthermore, we found that the imaginary part of the reflection coefficient is proportional to the energy storage in the near field of the cavity termination. From the calculation of this phase pick up, one can correctly predict both the position and shape of the MDM cavity transmission resonances over a wide range of wavelength and geometric parameters. The results agree very well with full-field FDFD simulations. The dependence of the quality factor on the length of the cavity shows that these resonances are reflection loss limited even at very small dielectric thickness and suggests the possibility of further improving the quality factor of these resonances by end face shaping.

APPENDIX A: DERIVATION OF THE REFLECTION COEFFICIENT

For calculating the reflection coefficient we primarily use two boundary conditions; the continuity of the z-directed electric field and the continuity of the total integrated x-directed poynting flux. In all the derivations the fields are invariant in y-direction and variation along x-direction is implicit. With the same definitions as in the main text we have for the continuity of the electric field,

$$(1+r)E_z^{\mathrm{sp}} = E_z^{\mathrm{fs}}. \tag{A1}$$

We also have from the continuity of the H-field,

$$(1-r)H_y^{\mathrm{sp}} = H_y^{\mathrm{fs}}. \tag{A2}$$

For the continuity of the x-directed poynting flux we have,

$$\int S_x^{cav} dz = \int S_x^{\mathrm{fs}} dz, \tag{A3}$$

which gives

$$\begin{aligned} &-(1+r)(1-r^*)\int_{-\infty}^{\infty} E_z^{\mathrm{sp}} H_y^{*\mathrm{sp}} dz \\ &= -\int_{-\infty}^{\infty} H_y^{\mathrm{fs}*} E_z^{\mathrm{fs}} dz. \end{aligned} \tag{A4}$$

Expressing the free space electric field in terms of Fourier transformed quantities, we can write

$$E_z^{\mathrm{fs}} = \int f(k_z) e^{ik_z z} dk_z \tag{A5}$$

$$= \int f(u) e^{ik_0 u z} k_0 du. \tag{A6}$$

substituting for E_z^{fs} from Eq. (A1) and solving for $f(k_z)$, we get

$$f(k_z) = \frac{(1+r)}{2\pi} \int_{-\infty}^{\infty} E_z^{\mathrm{sp}} e^{-ik_z z} dz \tag{A7}$$

$$= \frac{(1+r)}{2\pi} \int_{-\infty}^{\infty} E_z^{\mathrm{sp}} e^{-ik_0 u z} dz \tag{A8}$$

$$f(u) = \frac{1+r}{2\pi} I_1(u), \tag{A9}$$

where $k_z = k_0 u$ and $k_0 = \frac{2\pi}{\lambda}$ with

$$I_1(u) = \int E_z^{\mathrm{sp}} e^{-ik_z z} dz = \int E_z^{\mathrm{sp}} e^{-ik_0 u z} dz. \tag{A10}$$

We can now use Maxwell's equations to derive H_y^{fs} in terms of the Fourier component terms as

$$H_y^{\mathrm{fs}} = \frac{-1}{\omega\mu_0} \int_{-\infty}^{\infty} \frac{(1+r)I_1}{2\pi} \frac{k_0^2 e^{ik_z z}}{\sqrt{k_0^2 - k_z^2}} dk_z. \tag{A11}$$

Now, for the poynting flux balance we have

$$\int S_x^{\mathrm{fs}} dz = -\int E_z^{\mathrm{fs}} H_y^{\mathrm{fs}*} dz \tag{A12}$$

$$= -(1+r) \int E_z^{\mathrm{sp}} H_y^{\mathrm{fs}*} dz. \tag{A13}$$

Now substituting from Eq. (A11) and simplifying with Eq. (A10), we get

$$\int S_x^{\mathrm{fs}} dz = \frac{(1+r)(1+r^*)}{2\pi\omega\mu_0} \int \frac{|I_1|^2 k_0^2}{\sqrt{k_0^2 - k_z^2}} dk_z. \tag{A14}$$

Finally, substituting this back on to Eq. (A4) and simplifying, we get

$$\frac{(1-r^*)}{(1+r^*)} = \frac{1}{\lambda\sqrt{\frac{\mu_0}{\epsilon_0}} \int E_z^{\mathrm{sp}} H_y^{*\mathrm{sp}} dz} \int \frac{-|I_1|^2}{\sqrt{1-u^2}} du. \tag{A15}$$

APPENDIX B: ENERGY STORED IN THE NEAR FIELD

The energy stored in the near field has contributions from the electric and magnetic fields. For the energy stored in the electric field, W_E, we can write

$$W_E = \int \frac{1}{4} \epsilon_0 |E|^2 dV \tag{B1}$$

$$= \int \frac{1}{4} \epsilon_0 (|E_z|^2 + |E_x|^2) dV. \tag{B2}$$

From the derivation of the reflection coefficient, we have

$$E_z^{\mathrm{fs}} = \int_{-\infty}^{\infty} \frac{1+r}{2\pi} I_1 e^{ik_z z} e^{i\sqrt{k_0^2-k_z^2}x} dk_z. \tag{B3}$$

For the near fields, we have

$$E_{zNF}^{\mathrm{fs}} = \int_{k_z^2>k_0^2} \frac{1+r}{2\pi} I_1 e^{ik_z z} e^{i\sqrt{k_0^2-k_z^2}x} dk_z. \tag{B4}$$

Also, from $\nabla \cdot E = 0$

$$E_x^{\mathrm{fs}} = -\int_{-\infty}^{\infty} \frac{1+r}{2\pi} \frac{I_1}{\sqrt{k_0^2-k_z^2}} e^{ik_z z} e^{i\sqrt{k_0^2-k_z^2}x} dk_z, \tag{B5}$$

$$E_{xNF}^{\mathrm{fs}} = -\int_{k_z^2>k_0^2} \frac{1+r}{2\pi} \frac{I_1}{\sqrt{k_0^2-k_z^2}} e^{ik_z z} e^{i\sqrt{k_0^2-k_z^2}x} dk_z. \tag{B6}$$

We can rewrite the expression for the near-field energy using Fourier-transformed quantities,

$$W_{\mathrm{NF},E} = \int \frac{1}{4}\epsilon_0 |E_{\mathrm{NF}}|^2 dV = \int \frac{1}{4}\epsilon_0 |E_{\mathrm{NF}}|^2 dx dz, \tag{B7}$$

$$= \frac{1}{4\pi^2} \int \frac{1}{4}\epsilon_0 |F(E_{\mathrm{NF}})|^2 dk_x dk_z. \tag{B8}$$

For the Fourier transforms of the near fields, we have

$$F(E_{\mathrm{NF}}) = \int_{-\infty}^{\infty} E_{\mathrm{NF}} e^{ik_x x} e^{ik_z z} dz dx. \tag{B9}$$

Substituting from Eq. (B4) and writing $e^{i\sqrt{k_0^2-k_z^2}}$ as $e^{-\sqrt{k_z^2-k_0^2}}$, we get after simplification

$$F(E_{zNF}) = \frac{(1+r)I_1(k_z)}{\sqrt{k_z^2-k_0^2}+ik_x}, \quad |k_z| > k_0,$$
$$= 0, \quad |k_z| < k_0. \tag{B10}$$

We can now calculate the energy stored in the nearfield in E_z^{fs} as

$$W_{\mathrm{NF},E_z^{\mathrm{fs}}} = \frac{\epsilon_0}{16\pi^2} \int |F(E_{z\mathrm{NF}})|^2 dk_z dk_x$$
$$= \frac{\epsilon_0|1+r|^2}{16\pi^2} \int_{|k_z|=k_0}^{\infty} dk_z \int_{k_x=-\infty}^{\infty} dk_x \frac{|I_1(k_z)|^2}{k_z^2-k_0^2+k_x^2} \tag{B11}$$

$$= 2\frac{\epsilon_0|1+r|^2}{16\pi^2} \int_{k_z=k_0}^{\infty} dk_z \int_{k_x=-\infty}^{\infty} dk_x \frac{|I_1(k_z)|^2}{k_z^2-k_0^2+k_x^2} \tag{B12}$$

$$= \frac{\epsilon_0|1+r|^2}{8\pi^2} \int_{k_z=k_0}^{\infty} dk_z \frac{|I_1(k_z)|^2\pi}{\sqrt{(k_z^2-k_0^2)}} \tag{B13}$$

$$= \frac{\epsilon_0|1+r|^2}{8\pi} \int_{k_z=k_0}^{\infty} dk_z \frac{|I_1(k_z)|^2}{\sqrt{(k_z^2-k_0^2)}}. \tag{B14}$$

Similarly for the E_x^{fs} field we get

$$W_{\mathrm{NF},E_x^{\mathrm{fs}}} = \frac{\epsilon_0|1+r|^2}{8\pi} \int_{k_z=k_0}^{\infty} dk_z \frac{|I_1(k_z)|^2 k_z^2}{(k_z^2-k_0^2)^{3/2}}. \tag{B15}$$

The calculation for the energy in the magnetic field can be performed similarly, and we get

$$W_{\mathrm{NF},H_y^{\mathrm{fs}}} = \frac{\epsilon_0|1+r|^2}{8\pi} \int_{k_z=k_0}^{\infty} dk_z \frac{|I_1(k_z)|^2 k_0^2}{(k_z^2-k_0^2)^{3/2}}. \tag{B16}$$

Now we can write the total energy in the near field as,

$$W_{\mathrm{NF}} = W_{\mathrm{NF}}, H_y^{\mathrm{fs}} + W_{\mathrm{NF}}, E_x^{\mathrm{fs}} + W_{\mathrm{NF}}, E_z^{\mathrm{fs}}$$
$$= \frac{\epsilon_0|1+r|^2}{8\pi} \int_{k_z=k_0}^{\infty} dk_z \frac{|I_1(k_z)|^2}{\sqrt{k_z^2-k_0^2}} \left(1 + \frac{k_z^2+k_0^2}{k_z^2-k_0^2}\right) \tag{B17}$$

$$= \frac{\epsilon_0|1+r|^2}{8\pi} \int_{k_z=k_0}^{\infty} dk_z \frac{|I_1(k_z)|^2}{\sqrt{k_z^2-k_0^2}} \left(2 + \frac{2k_0^2}{k_z^2-k_0^2}\right) \tag{B18}$$

$$= \frac{\epsilon_0|1+r|^2}{4\pi} \int_{u=1}^{\infty} du \frac{|I_1(u)|^2}{\sqrt{u^2-1}} \left(1 + \frac{1}{u^2-1}\right), \tag{B19}$$

Where $u = \frac{k_z}{k_0}$.

Also from above, we can verify that

$$W_e - W_m = W_{\mathrm{NF},E_x^{\mathrm{fs}}} + W_{\mathrm{NF},E_z^{\mathrm{fs}}} - W_{\mathrm{NF},H_y^{\mathrm{fs}}}$$
$$= \frac{\epsilon_0|1+r|^2}{4\pi} \int_{u=1}^{\infty} du \frac{|I_1(u)|^2}{\sqrt{u^2-1}}. \tag{B20}$$

---

[1] H. Yokota, K. Saito, and T. Yanagida, Phys. Rev. Lett. **80**, 4606 (1998).

[2] B. Pettinger, B. Ren, G. Picardi, R. Schuster, and G. Ertl, Phys. Rev. Lett. **92**, 096101 (2004).

[3] B. Pettinger, A. Tadjeddine, and D. Kolb, Chem. Phys. Lett. **66**, 544 (1979).

[4] M. Righini, G. Volpe, C. Girard, D. Petrov, and R. Quidant, Phys. Rev. Lett. **100**, 186804 (2008).

[5] C. J. Chen and R. M. Osgood, Phys. Rev. Lett. **50**, 1705 (1983).

[6] L. Cao, D. N. Barsic, A. R. Guichard, and M. L. Brongersma, Nano Lett. **7**, 3523 (2007).

[7] Y. C. Jun, R. Pala, and M. L. Brongersma, J. Phys. Chem. C **114**, 7269 (2010).

[8] R. M. Bakker, H.-K. Yuan, Z. Liu, V. P. Drachev, A. V. Kildishev, V. M. Shalaev, R. H. Pedersen, S. Gresillon, and A. Boltasseva, Appl. Phys. Lett. **92**, 043101 (2008).

[9] J. N. Farahani, D. W. Pohl, H.-J. Eisler, and B. Hecht, Phys. Rev. Lett. **95**, 017402 (2005).

[10] T. H. Taminiau, R. J. Moerland, F. B. Segerink, L. Kuipers, and N. F. van Hulst, Nano Lett. **7**, 28 (2007).

[11] W. Cai, J. S. White, and M. L. Brongersma, Nano Lett. **9**, 4403 (2009).

[12] T. Nikolajsen, K. Leosson, and S. I. Bozhevolnyi, Appl. Phys. Lett. **85**, 5833 (2004).

[13] A. V. Krasavin and N. I. Zheludev, Appl. Phys. Lett. **84**, 1416 (2004).

[14] H. A. A. Domenico Pacifici and H. J. Lezec, Nat. Photon. **1**, 402 (2007).

[15] A. Hryciw, Y. C. Jun, and M. L. Brongersma, Nat. Mater. **9**, 3 (2010).

[16] R. J. Walters, R. V. A. van Loon, I. Brunets, J. Schmitz, and A. Polman, Nat. Mater. **9**, 21 (2010).

[17] H. T. Miyazaki and Y. Kurokawa, Appl. Phys. Lett. **89**, 211126 (2006).

[18] H. T. Miyazaki and Y. Kurokawa, Phys. Rev. Lett. **96**, 097401 (2006).

[19] J. S. White, G. Veronis, Z. Yu, E. S. Barnard, A. Chandran, S. Fan, and M. L. Brongersma, Opt. Lett. **34**, 686 (2009).

[20] T. Ishi, J. Fujikata, K. Marita, T. Baba, and K. Ohashi, Jpn. J. Appl. Phys. **44**, L364 (2005).

[21] Y. C. Jun, K. C. Y. Huang, and M. L. Brongersma, Nat. Commun. **2**, 283 (2011).

[22] P. Neutens, P. Van Dorpe, I. De Vlaminck, L. Lagae, and G. Borghs, Nat. Photon. **3**, 283 (2009).

[23] S. I. Bozhevolnyi and T. Søndergaard, Opt. Express **15**, 10869 (2007).

[24] L. Novotny, Phys. Rev. Lett. **98**, 266802 (2007).

[25] T. Søndergaard and S. Bozhevolnyi, Phys. Rev. B **75**, 073402 (2007).

[26] G. W. Bryant, F. J. Garcia de Abajo, and J. Aizpurua, Nano Lett. **8**, 631 (2008).

[27] T. Sondergaard, J. Beermann, A. Boltasseva, and S. I. Bozhevolnyi, Phys. Rev. B **77**, 115420 (2008).

[28] E. S. Barnard, J. S. White, A. Chandran, and M. L. Brongersma, Opt. Express **16**, 16529 (2008).

[29] H. A. Jamid and S. J. Albader, IEEE Photon. Tech. Lett. **7**, 321 (1995).

[30] T. Leskova and N. Gapotchenko, Solid State Commun. **53**, 351 (1985).

[31] T. Leskova, A. Maradudin, and W. Zierau, Opt. Commun. **249**, 23 (2005).

[32] R. Zia, A. Chandran, and M. L. Brongersma, Opt. Lett. **30**, 1473 (2005).

[33] R. Gordon, Phys. Rev. B **73**, 153405 (2006).

[34] J. A. Porto, F. J. Garcia-Vidal, and J. B. Pendry, Phys. Rev. Lett. **83**, 2845 (1999).

[35] R. Zia, M. D. Selker, P. B. Catrysse, and M. L. Brongersma, J. Opt. Soc. A **21**, 2442 (2004).

[36] J. A. Dionne, L. A. Sweatlock, H. A. Atwater, and A. Polman, Phys. Rev. B **72**, 075405 (2005).

[37] E. Economou, Phys. Rev. **182**, 539 (1969).

[38] Z. Szentirmay, Phys. Rev. B **36**, 2607 (1987).

[39] *Plasmonic Nanoguides and Circuits*, edited by S. I. Bozhevolnyi (Pan Stanford, Singapore, 2009).

[40] Ş. E. Kocabaş, G. Veronis, D. A. B. Miller, and S. Fan, Phys. Rev. B **79**, 035120 (2009).

[41] G. Hernandez, *Fabry-Perot Interferometers* (Oxford University Press, Oxford, 1986).

[42] Y. Takakura, Phys. Rev. Lett. **86**, 5601 (2001).

[43] J. D. Jackson, *Classical Electrodynamics*, 3rd ed. (Wiley, New York, 1999).

[44] P. Lalanne, J. P. Hugonin, and J. C. Rodier, Phys. Rev. Lett. **95**, 263902 (2005).

[45] S. Fan, *Surface Plasmon Nanophotonics*, Vol. 12 of Springer Series in Optical Sciences (Springer, Dordrecht, 2007), pp. 169–182.

[46] A. Rakic, A. Djurisic, J. Elazar, and M. Majewski, Appl. Opt. **37**, 5271 (1998).

[47] Y. C. Jun, R. D. Kekatpure, J. S. White, and M. L. Brongersma, Phys. Rev. B **78**, 153111 (2008).